POLITECNICO
MILANO 1863

SCUOLA DI INGEGNERIA INDUSTRIALE
E DELL'INFORMAZIONE

EXECUTIVE SUMMARY OF THE THESIS

Lightweight solutions for High Manganese steel

TESI MAGISTRALE IN MECHANICAL ENGINEERING – INGEGNERIA MECCANICA

AUTHOR: XUWEI XU

ADVISOR: PROF. CARLO MAPELLI

ACADEMIC YEAR: 2025-2026

Introduction

The demand for lightweight structural materials has grown significantly in recent decades, driven by the need to improve energy efficiency, reduce emissions, and enhance performance in sectors such as transportation, construction, and power generation. Steels remain the most widely used structural materials due to their favourable balance of strength, toughness, and cost. Among them, high manganese steels are particularly attractive because of their good ductility, toughness, and work hardening capacity, which enable them to withstand demanding mechanical and impact-loading conditions. However, their relatively high density poses a limitation for applications where weight reduction is critical. To address this challenge, research has increasingly focused on developing strategies that reduce the weight of high manganese steels while maintaining their outstanding mechanical properties. Two main approaches have emerged: The first involves alloy design through the incorporation of low-density elements, such as aluminium, which significantly reduces density while potentially improving oxidation and corrosion behaviour. Nevertheless, Al additions also introduce microstructural complexities that can influence phase stability, ductility, and processing. Understanding and optimizing these effects are important to fully exploit the benefits of aluminium alloying in high manganese steels. However, this approach is not universally applicable. In certain environments, such as nuclear reactors, aluminium is restricted, and it requires the addition of chromium for high temperature application. In such cases, the density of high-manganese steel becomes a fixed constraint, and alternative approaches are necessary. The second strategy draws inspiration from nature and focuses on structural design. By introducing bioinspired geometries, such as cellular, lattice, or hierarchical structures, the effective weight of components can be reduced without compromising their mechanical performance. This approach leverages advances in computational design, additive manufacturing, and materials engineering, enabling high-manganese steels to be used in lightweight architectures with optimized stiffness, strength, and energy absorption capabilities. This thesis explores both pathways for lightweight design in high-manganese steels. Special focus is placed on the role of aluminium addition in modifying

material properties and on the potential of bioinspired geometrical optimization to unlock new applications.

1. Overview on High Mn steel

Manganese is highlighted as a key alloying element in steelmaking due to its low cost and multifunctional role. At moderate contents, Mn increases strength and toughness, while at high concentrations (>10 wt.%) it stabilizes the austenitic phase at room temperature, leading to exceptional ductility, toughness, and strain-hardening capability. These properties arise from deformation mechanisms such as transformation-induced plasticity (TRIP) and twinning-induced plasticity (TWIP). However, the relatively high density of high-Mn steels limits their use in weight-critical applications, motivating the development of low-density variants.

1.1. Fe-Mn-Al-C steel

Fe–Mn–Al–C steels are introduced as a promising solution for lightweight design. Aluminium plays a central role by reducing density by approximately 1.3% per 1 wt.% addition, allowing density reductions of up to ~10% while maintaining high strength. Aluminium also improves oxidation and corrosion resistance, although excessive Al can reduce ductility and complicate processing due to ferrite stabilization and ordered phase formation. Manganese and carbon counterbalance this effect by stabilizing austenite, enabling a wide range of microstructures including ferritic, duplex, and fully austenitic steels, as shown in Table 1.1. These microstructural classes exhibit diverse mechanical properties, from moderate strength ferritic alloys to highly ductile austenitic steels with ultimate tensile strengths exceeding 1 GPa.

The effects of Mn and Al additions on the Fe–C phase diagram are analyzed, showing significant shifts in phase stability, eutectoid temperature, and carbide formation. Particular attention is given to the κ-carbide phase, a perovskite type $(Fe,Mn)_3AlC$ compound that forms coherently with austenite.

κ-carbides play a crucial role in precipitation strengthening but may also induce embrittlement depending on their morphology, distribution, and interface coherence.

Processing routes for Fe–Mn–Al–C steels are reviewed, highlighting challenges related to hot workability, segregation, and κ-carbide precipitation. Strategies such as controlled hot rolling, rapid cooling, solution treatment, and aging are discussed as means to tailor microstructure and mechanical performance.

Both hot- and cold-working routes are considered, depending on whether the alloy is ferritic, duplex, or austenitic.

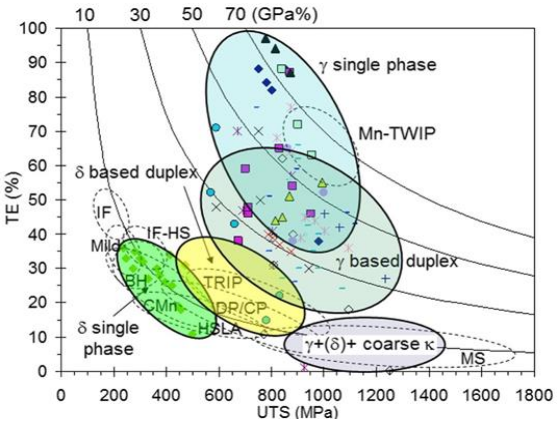

Figure 1.1 Plot of total elongation vs ultimate tensile strength in Fe-Mn-Al-C alloys.

	Al [wt.%]	Mn [wt.%]	C [wt.%]	σ_{UTS} [MPa]	ϵ [%]
Ferritic (α)	5–9%	< 5%	<0.05%	200–600	10–40
Ferrite based duplex	3–7%	2–12%	0.05–0.5%	400–900	10–40
Austenite based duplex	5–10%	5–30%	0.4–0.7%	800–1300	10–40
Austenite (γ)	5–12%	12–30%	0.6–2.0%	800–1500	30–80

Table 1.1 Types of Fe-Mn-Al-C steel depending on chemical composition [4].

Finally, the mechanical behaviour of Fe–Mn–Al–C steels is summarized. Strengthening mechanisms include solid-solution strengthening, precipitation hardening by κ-carbides, and advanced deformation mechanisms governed by stacking fault energy. Depending on composition, these steels can exhibit TRIP, TWIP, microband-induced plasticity, or shear-band-related mechanisms, enabling an exceptional combination of strength, ductility, and strain hardening. Corrosion behaviour is also addressed, noting that while Fe–Mn–Al–C steels do not match stainless steels, they outperform conventional carbon steels, especially with optimized Al content and austenitic microstructures.

2. Materials and methods

Two complementary strategies for achieving lightweight structures are discussed. The first is material selection, focusing on materials with high specific properties, such as high specific strength and stiffness. Material selection charts (Figure 2.1) are introduced as a graphical tool for comparing material families based on performance indices normalized by density. Within this context, Fe–Mn–Al–C steels discussed in the previous chapter are identified as promising candidates due to their excellent strength-to-weight ratios.

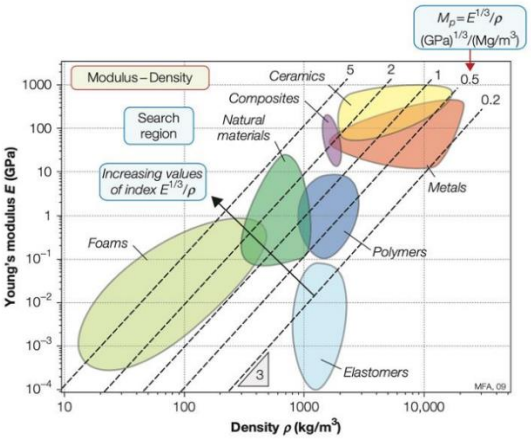

Figure 2.1 Material selection charts

The second strategy is geometric optimization, which emphasizes that structural efficiency depends not only on material properties but also on shape and architecture. Three optimization approaches are outlined: topology optimization, sizing optimization, and shape optimization. This thesis focuses on shape-driven optimization through bioinspired structural morphologies, aiming to combine efficient materials with efficient geometries to maximize mechanical performance per unit mass.

2.1. Bioinspired design

Bioinspired design is introduced as a systematic approach to overcoming limitations of conventional engineering structures by learning from nature. Rather than direct imitation, the methodology relies on abstracting functional principles from biological systems and translating them into engineering solutions.

The adopted bioinspired design pathway consists of eight steps. First, the engineering problem is defined as improving the compressive performance and stiffness-to-weight ratio of hollow cylindrical structures. Second, the problem is functionally abstracted into mechanical requirements such as load-bearing capacity and deformation control under axial compression. Third, biological systems that experience similar loading conditions are explored. Fourth, suitable biological analogues are selected. Fifth, candidate models are evaluated for relevance and feasibility. Sixth, structural principles are extracted from the biological model. Seventh, these principles are assessed for manufacturability using available technologies. Finally, the bioinspired concepts are implemented and validated through numerical simulations and experimental testing.

This structured methodology ensures that biological inspiration is applied in a controlled, engineering-oriented manner rather than in a purely conceptual or aesthetic way.

2.1.1. Bio inspirational sources

The primary biological model selected in this work is the skeleton of the cholla cactus (genus *Cylindropuntia*). When the soft tissues of the cactus decay, a rigid, porous wooden skeleton remains, composed of interconnected hollow cylindrical elements. These skeletal structures exhibit a remarkable combination of low mass and high compressive load-bearing capacity.

The mechanical efficiency of the cholla skeleton arises from its hierarchical porous architecture. The structure consists of lignified vascular bundles forming a reticulated network, while large voids remain between these bundles.

Figure 2.2 Cholla cactus wood skeletons

Lignin-rich xylem provides compressive stiffness, whereas the voids significantly reduce weight without critically compromising mechanical integrity. This architecture enables the cactus to support its own weight and withstand environmental loads such as wind.

The pore geometry varies both between species and along the length of individual cactus stalks. Elongated or circular perforations influence local stress distribution and stiffness. From an engineering perspective, these features suggest that controlled porosity and pore shape can be used to tune mechanical properties such as axial stiffness and shear resistance. This natural example demonstrates an optimized balance between material usage and structural performance, making it a suitable template for lightweight cylindrical structures.

2.2. Design of the structures

The reference geometry is a thin-walled hollow cylinder defined by height, external diameter, and wall thickness. Bioinspired variants are generated by introducing regularly distributed pores into the cylindrical wall. The pores are designed with a linear slot-like shape, approximating the elongated perforations observed in cactus skeletons.

Key design parameters include cylinder height, external diameter, wall thickness, pore radius, and centre-to-centre spacing between pores. The cylinder height is fixed at 110 mm, while wall thickness and diameter are selected based on experimental observations of natural cactus skeletons. Pore geometry and spacing are varied to explore their influence on stiffness and load-bearing behaviour.

Pore circularity is introduced as a quantitative descriptor of pore shape. Previous studies on cactus-inspired structures have shown that pore circularity and wall thickness-to-diameter ratio

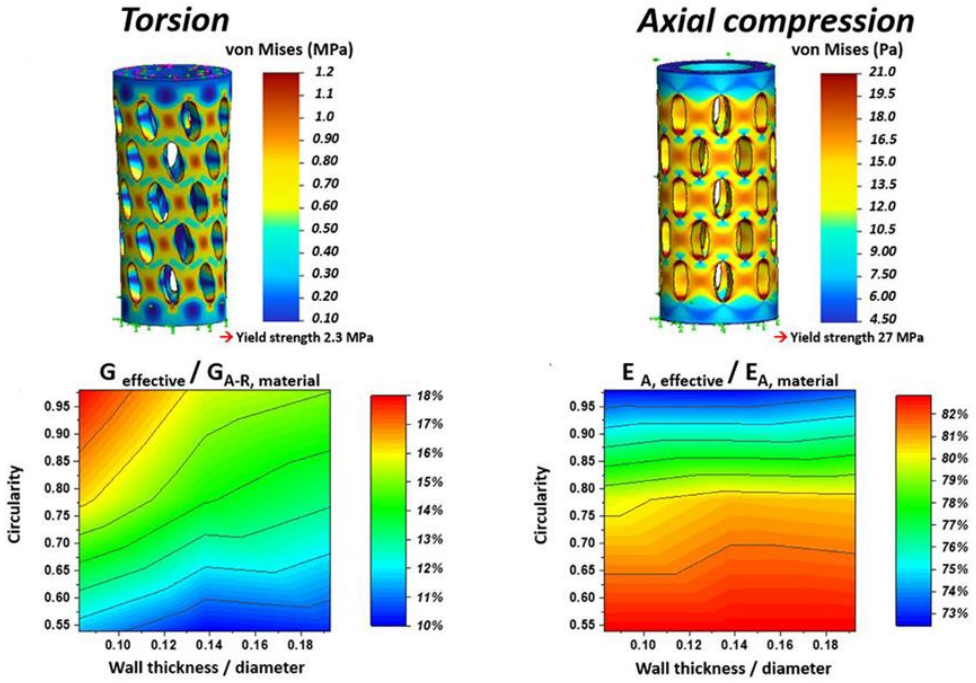

Figure 2.3 Finite element analysis of cactus skeleton inspired structures by varying pore circularity and wall thickness. On the left, results of torsion simulations with the corresponding heat map are shown (the colour intensity reflects the effective stiffness as a percentage of the prescribed material stiffness), while on the right, results of compression simulation are shown.

strongly influence axial and shear stiffness (Figure 2.3). Lower pore circularity tends to improve axial compressive stiffness, while higher circularity benefits shear stiffness. The natural cactus skeleton appears to adopt an intermediate pore geometry that balances these competing requirements, suggesting an evolutionary optimization for combined loading conditions.

Using these insights, multiple structural configurations are generated, ranging from uniformly distributed pores to more advanced arrangements with alternating or tilted pores.

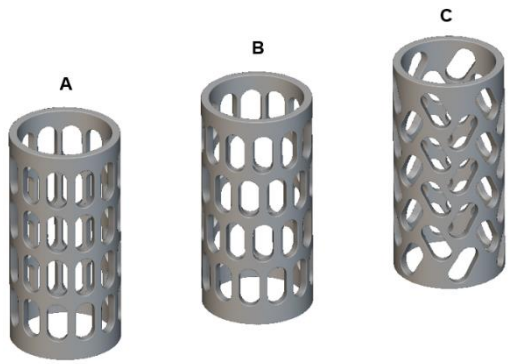

Figure 2.4 Cellular structures created with Ntopology

2.3 Numerical methods

Numerical simulations are employed to predict the mechanical behaviour of the designed structures prior to experimental testing. Finite element analysis is used to evaluate stress distribution, deformation patterns, stiffness, and load-bearing capacity under axial compression. Special attention is given to mesh convergence to ensure numerical accuracy.

The 3 configurations are compared under 5mm displacement compression simulation with identical boundary conditions, allowing for direct assessment of the effect of bioinspired geometry.

2.4 Experimental methods

Additive manufacturing is first employed to produce sacrificial patterns of the designed structures. These patterns are then used in investment casting to fabricate metallic components from the selected high-manganese alloy. This hybrid approach allows the realization of complex geometries while maintaining compatibility with industrial casting processes.

Compression tests are conducted under quasi-static loading to evaluate stiffness, peak load, and deformation modes. These tests provide direct experimental evidence of the effectiveness of the bioinspired designs.

Finally, metallographic analyses are performed to assess microstructural features, defect distribution, and casting quality.

3. Material characterization

The study builds upon previous work conducted on high-manganese stainless steels, particularly an alloy referred to as Alloy 2, which was previously characterized in detail by Capitanio and Carlesso. This alloy exhibits strong similarities to the newly developed alloy examined in the present thesis and is therefore used as a reference material. Its experimentally validated mechanical properties are employed as input data for preliminary numerical simulations performed using Abaqus and COMSOL, enabling reliable early-stage modelling.

The referenced high-manganese alloys were designed as alternatives to conventional nickel-containing stainless steels, with manganese acting as a partial or complete substitute for nickel. High manganese content stabilizes the austenitic phase at room temperature, enhances solid-solution strengthening, improves hot ductility, and promotes high work-hardening capacity. Chromium additions further enhance corrosion resistance by promoting the formation of a protective oxide layer, which is particularly relevant for demanding environments such as nuclear reactor systems.

Thermodynamic predictions and experimental investigations confirmed a predominantly FCC austenitic microstructure at room temperature, with minor ferrite content depending on solution treatment temperature and holding time. Solution heat treatments between 950 °C and 1050 °C effectively reduced grain-boundary precipitates, promoting chemical homogenization. Increasing temperature and holding time led to partial grain growth, increased ferrite fraction, and progressive dissolution of secondary phases, effects attributed to the slow diffusion of ferrite-stabilizing elements

such as chromium and niobium. Optical microscopy and electron microscopy confirmed the coexistence of austenite and ferrite and revealed the sensitivity of precipitate morphology and distribution to thermal history.

Mechanical characterization demonstrated an excellent balance between strength and ductility. Hardness measurements indicated that higher solution temperatures reduced hardness due to precipitate dissolution, while holding time had a limited net effect. Tensile testing of hot-rolled and solution-treated specimens revealed high ultimate tensile strength combined with large uniform elongation and pronounced strain-hardening behaviour. Fractographic analysis showed predominantly ductile fracture, with localized microcracking associated with secondary phases or defects, highlighting the importance of microstructural control.

3.1. The new High Mn alloy

The newly developed high-manganese, high-chromium alloy investigated in this thesis was designed to further enhance austenite stability, corrosion resistance, and solid-solution strengthening. The alloy was produced in the as-cast condition and subsequently solution treated at 1050°C followed by water quenching.

Thermocalc predicted a complex phase evolution, with ferrite and σ phase dominating at low temperatures and austenite becoming stable above approximately 450–500 °C. At the selected solution treatment temperature, the alloy lies within an austenite–ferrite two-phase field, with austenite as the dominant phase and only a minor fraction of carbides. This processing route is therefore effective in dissolving brittle intermetallic phases and homogenizing the as-cast microstructure.

Light Optical Microscopy of the solution-treated alloy revealed a predominantly austenitic matrix composed of equiaxed grains with a homogeneous size distribution, as shown in Figure 3.1, indicating effective recrystallization during heat treatment.

Casting related porosity and inclusions were observed as dark rounded features dispersed throughout the microstructure. Quantitative image analysis of a representative optical micrograph yielded an estimated porosity of approximately 0.94%, a value considered acceptable for cast structural components, though further analysis across multiple sections would be required for full statistical validation.

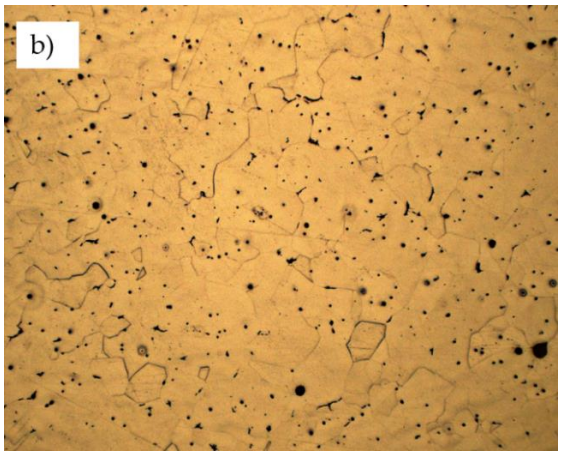

Figure 3.1 Novel alloy microstructure images taken with optical microscope at 20x

Scanning Electron Microscopy combined with Energy Dispersive X-ray Spectroscopy provided detailed insight into the microstructural constituents. The matrix phase was confirmed to be a chemically homogeneous γ-austenitic solid solution, with manganese and chromium contents closely matching the nominal alloy composition. Chromium-enriched particles were identified along grain boundaries, consistent with σ-phase formation, while finer intragranular precipitates with moderate chromium enrichment were attributed to a combination of σ phase and M23C6 carbides. These observations are in good agreement with thermodynamic predictions and confirm that, despite solution treatment, limited amounts of secondary phases remain present.

%wt	Fe	C	Mn	Cr	Si	Ni	V	Nb	Mo
Alloy	60.19	0.22	21.47	17.57	0.47	0.23	0.084	0.104	0.046

Table 3.1 Chemical composition of the new High manganese alloy

4. Results and discussion

This chapter presents and analyses the outcomes of both the numerical simulations and experimental investigations conducted in this work. The first section focuses on the finite element analyses performed using Abaqus, in which key mechanical and structural parameters were evaluated through simulation plots. These results are then compared with those obtained from COMSOL.
Subsequently, the chapter presents the results of manufacturing process regarding with the cast samples, beginning with pattern fabrication via 3D printing, followed by the investment casting procedure. The resulting cast components are then examined to evaluate their dimensional accuracy and surface quality. Finally, the experimental compression tests performed on the cast specimens are presented and discussed, enabling a direct comparison between the numerical predictions and the measured mechanical performance of the samples.

4.1. Numerical simulation results

To establish a direct benchmark for the compressive performance of the bioinspired structures, a numerical simulation was conducted on a conventional hollow cylinder with identical height, external diameter, and material volume. While the hollow cylinder exhibits a higher initial stiffness, as reflected by a steeper initial reaction force-displacement response, its mechanical behaviour becomes highly unstable once yielding occurs. At approximately 1 mm of displacement, thin-wall buckling initiates, leading to a sudden loss of load-bearing capacity and pronounced oscillations in reaction force. This instability contrasts sharply with the more stable post-yield response observed in the bioinspired configurations, highlighting the effectiveness of geometric optimization in delaying structural collapse.
Comparative analysis among the bioinspired designs reveals distinct mechanical responses governed by structural topology. Configurations A and B demonstrate nearly identical behaviour during the initial and intermediate loading stages, reaching a comparable peak reaction force of approximately 68 kN at 1.8 mm displacement. Both configurations ultimately develop an asymmetric lateral buckling mode under loading.
In contrast, configuration C displays a lower reaction force throughout the entire displacement range. Its behaviour is dominated by a more compliant, spring-like deformation mode, enabling progressive strain accommodation without the occurrence of buckling.

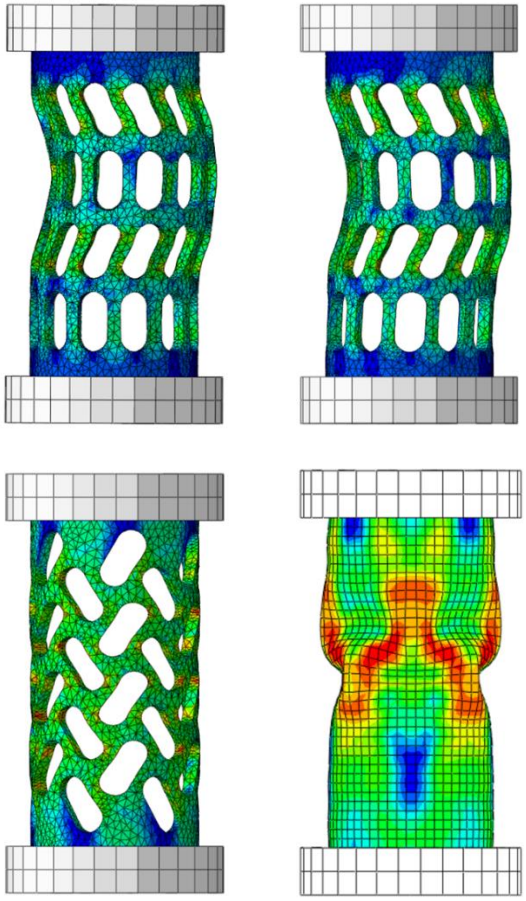

Figure 4.1 Deformed structure under 5mm vertical displacement, respectively: conf. A, conf. B, conf. C and reference hollow cylinder.

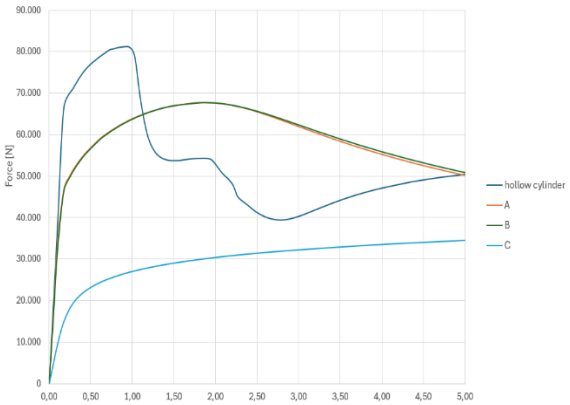

Figure 4.2 Reaction force curves of the hollow cylinder and the 3 different configurations

4.2. Experimental results

The numerical simulations provided a first prediction of the mechanical response of the proposed bioinspired structures; nevertheless, an experimental validation is essential to assess their real behaviour. This chapter therefore presents the results of the experimental campaign conducted on the structures manufactured by investment casting. Initially, the geometrical fidelity of the cast components was evaluated by comparing the measured dimensions of the real specimens with the original CAD geometry, in order to quantify possible deviations introduced during the manufacturing process. The surface quality was assessed through a visual inspection, providing a qualitative evaluation of the overall surface finish and the presence of casting defects.

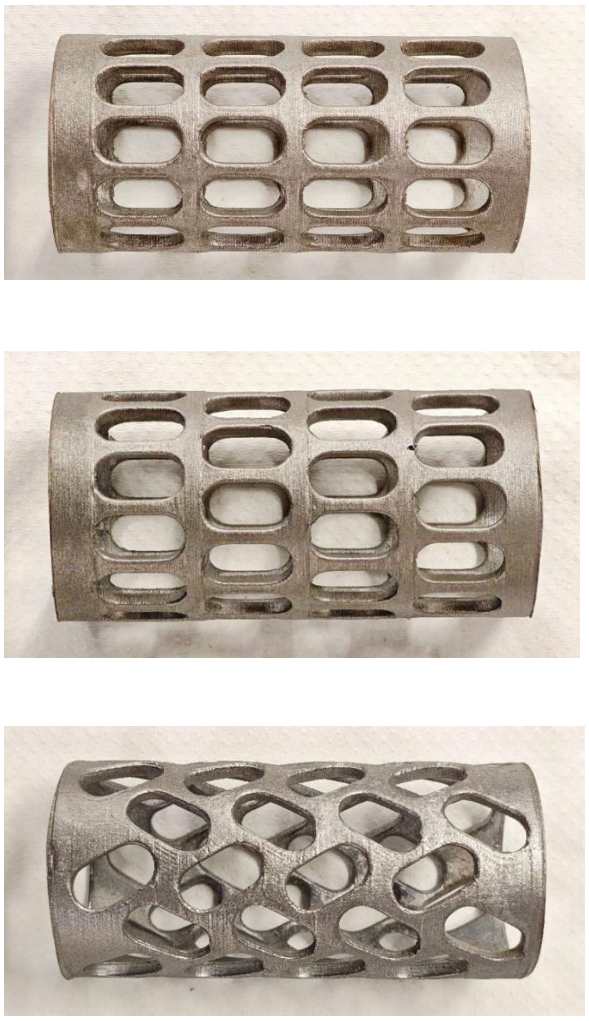

Figure 4.3 As cast bioinspired lattice structures

4.2.1. Compression test results

The experimental compression tests were used to validate the Abaqus simulations. The compression tests were first performed under an imposed displacement of 5 mm, consistently with the numerical model, analysing both the deformation modes and the reaction forces. The investigation was then extended to compression up to failure for all three structural configurations, allowing the assessment of their actual load-bearing capacity and collapse mechanisms.

Figure 4.4 Deformed structures under 5mm compression displacement.

The compression tests showed a remarkable agreement with the numerical predictions. In particular, the deformed shapes at a displacement of 5 mm were perfectly replicated in the real experiments, confirming that the simulation accurately captured the collapse mechanisms and the progressive deformation of the cellular architecture.

Figure 4.5 Deformed structures at failure

Configurations A and B exhibit a distinct lateral buckling mode, with asymmetric curvature developing along the cylinder's length. Their force-displacement response (Figure 4.6) shows an initial linear elastic region up to approximately 1.7 mm displacement, followed by a peak force of around 55 kN at 2.2 mm. Configuration C exhibits a uniform, symmetric deformation mode, with the lattice struts bending in-phase.
The overall behavior of Configuration C is characterized by a more gradual, distributed failure mode compared to Configurations A and B.

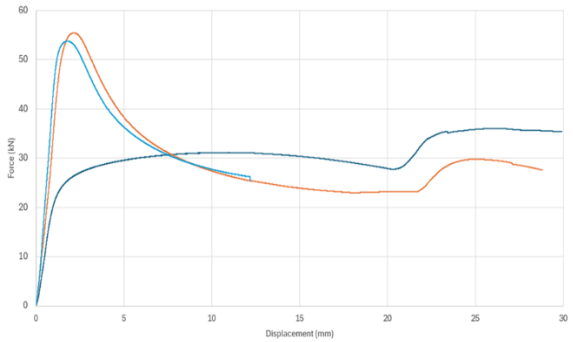

Figure 4.6 Comparison of reaction force curves of 3 configurations: Conf. A (light blue); Conf. B (orange); Conf. C (blue)

4.2.2. Microstructural analysis

Microstructural analysis of the deformed specimens was carried out to identify the active deformation mechanisms, such as slip bands, TWIP and/or TRIP (ε-martensite) effects, by means of light optical microscopy (LOM), with final confirmation provided by EBSD analysis to determine the crystallographic orientations and the corresponding phases present after deformation.

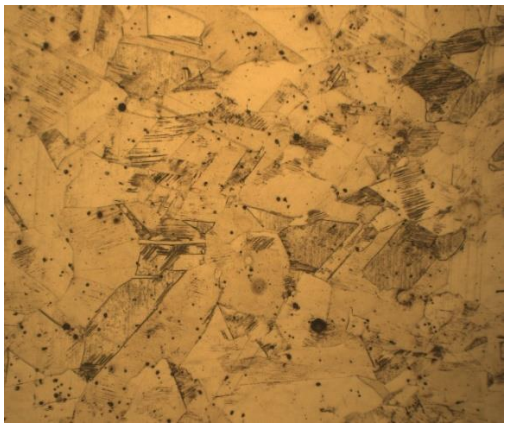

Figure 4.7 LOM images at 20x of deformed strut sample of Configuration B.

5. Conclusion

This thesis has investigated two complementary strategies for the development of lightweight high-manganese steels, addressing both alloy design and structural optimization in order to overcome the intrinsic density limitation of these materials. The study was motivated by the growing demand for structural solutions capable of combining high mechanical performance with mass reduction, particularly for applications in extreme environments, such as lead-cooled reactors, where conventional alloying approaches are constrained. Through the integration of materials science, bioinspired design, numerical modelling, and experimental validation, the work has demonstrated that lightweight design in high Mn steels can be effectively achieved by acting at the compositional and geometrical scales.

Bibliography

[1] D. W. Suh and N. J. Kim, "Low-density steels," Scripta Materialia, vol. 68, p. 337 338, 2013.

[2] S. Chen, R. Rana, A. Haldar and R. K. Ray, "Current state of fe-mn-al-c low density steels," Progress in Materials Science, vol. 89, p. 345–391, 2017.

[3] O.A.Zambrano, "A general perspective of Fe–Mn–Al–C steels," J Mater Sci, vol. 53, p. 14003–14062, 2018.

[4] Luca De Vivo, Albert K. Matsushita, Daniel Kupor, Josue Luna, Beatrice A. Tierra, Rober L. Sah and et al., "Cholla cactus frames as lightweight and torsionally tough biological materials," Acta Biomaterialia, vol. 112, p. 213–224 , 2020.